ELSEVIER

Computational Materials Science 28 (2003) 633–644

COMPUTATIONAL MATERIALS SCIENCE

www.elsevier.com/locate/commatsci

Determination of deformation and failure properties of ductile materials by means of the small punch test and neural networks

Martin Abendroth *, Meinhard Kuna

Institute of Mechanics and Fluid Dynamics, Freiberg University of Mining and Technology, Lampadiusstrae 4, D-09596 Freiberg, Germany

Abstract

This paper describes an approach to identify plastic deformation and failure properties of ductile materials. The experimental method of the small punch test is used to determine the material response under loading. The resulting load displacement curve is transferred to a neural network, which was trained using load displacement curves generated by finite element simulations of the small punch test and the corresponding material parameters. The simulated material behavior of the specimen is based on the ductile elastoplastic damage theory of Gurson, Tvergaard and Needleman. During a training process the neural network generates an approximated function for the inverse problem relating the material parameters to the shape of the load displacement curve of the small punch test. This technique was tested for three different materials (ductile steels). The identified parameters are verified by testing and simulating notched tensile specimens.

PACS: 02.70.Dh; 07.05.Tp; 46.50; 62.20.Mk; 81.40.Np; 81.70.Bt
Keywords: Small punch test; Neural network; Damage; Ductile fractue; Finite elements

1. Introduction

In recent years, different continuum damage models developed by Rice and Tracey, Gurson, Rousselier, Lemaitre, Chaboche etc. are widely accepted to describe ductile failure of metals. Usually, such models contain a set of parameters, which are unknown for the most ductile materials used in mechanical engineering.

The ductile material behavior in structural components is changing due to in service loading, aging, irradiation, embrittlement and some other influences. That requires an in situ monitoring of the material state. In order to determine material parameters at various locations e.g. in weldments or gradient materials, the size of the material taken out for a test specimen should be very small but representative.

In the small punch test (SPT), a disk like specimen of $\varnothing 8 \times 0.5$ mm size is deformed in a miniaturized deep drawing experiment. The measurable output is the load displacement curve of

* Corresponding author.
E-mail address: martin.abendroth@imfd.tu-freiberg.de (M. Abendroth).

0927-0256/$ - see front matter © 2003 Elsevier B.V. All rights reserved.
doi:10.1016/j.commatsci.2003.08.031

the punch, which contains information about the elasto-plastic deformation behavior and about the strength properties of the material.

Manahan et al. [1] introduced a disk bending test to determine post irradiation mechanical properties of materials used in the nuclear power industries [2,3]. Baik et al. [4,5] defined the area under the load displacement curve as small punch fracture energy and found correlations between results from Charpy-V-notch and small punch experiments determining the ductile to brittle transition temperature DBTT. The small punch test is often used to analyze irradiation effects [6–8]. Some researchers used the SPT to predict the elastic plastic properties [9] and the ductile fracture toughness J_{I_c} [10–13] or the brittle fracture toughness K_{I_c} [14]. Most recently a group [15] developed an inverse method for the estimation of the Ramberg–Osgood stress strain relation using the SPT load displacement curve. Huber et al. [16] showed that neural networks are suitable for the determination of constitutive properties from spherical indentation tests.

In the present paper, a new approach is established to identify the material parameters of hardening and damage. The load displacement curve is transferred to a neural network (NN) [17,18], which has been trained with load displacement curves generated by FEM-simulations of the SPT with the corresponding material parameters. The simulated material behavior of the specimen is based on the elastoplastic damage theory of Gurson, Tvergaard and Needleman (GTN-model) [19–21]. The output of the neural network is a set of material parameters describing hardening and damage behavior of the tested material. Subsequently, simulations of tensile tests, SENB- or CT-specimen can be performed predicting ductile crack growth behavior and material parameters of ductile fracture.

These identification procedure was performed for the steels 10MnMoNi55, StE-690, 18Ch2MFA that are widely used in mechanical engineering. The advantages and restrictions for applying this identification approach are discussed. An outlook to further improvements and research activities is given.

2. Experimental methods

The small punch test is performed using the device as seen in Fig. 1. The specimen is clamped between die and down-holder, which are supported by the bottom housing part. The screwable upper housing part is used to provide the clamping force. The punch driven by the cross-head plate of the testing machine deforms the specimen centrically. The punch displacement is measured parallel to the punch and close to the specimen to prevent errors due to the bending of the cross-head of the testing machine and other elastic deformations of the experimental setup. A load cell between cross-head and punch measures the force acting on the punch. The bottom face of the specimen can be observed by two CCD-cameras via a conical boring in the ground plate. A speckle pattern is sprayed on the bottom face of the specimen, so that the deformation field can be measured using a 3-dimensional grating method [22].

The results of this experiment are the load displacement curve of the punch and a deformation field as can be seen in Fig. 2. The load displacement curve can be divided into several parts. Part I is mainly controlled by the elastic properties of the material, Part II reflects the transition between the elastic and plastic behavior, Part III shows the hardening properties up to part IV where geometrical softening and damage occurs. During the steep decent in Part V the specimen fails and a crack grows circular around the center of the specimen. The remaining force in Part VI is needed to push the punch trough the already cracked specimen.

The small punch test was performed using specimens of three different steels. These are the grades 10MnMoNi55, 18Ch2MFA used often in nuclear power plants for pipes and pressure vessels and StE-690 a fine-grained high strength steel widely used in many fields of technology especially in civil engineering.

In order to verify the material parameters determined by the SPT, tensile tests with round notched specimens (Fig. 3) were carried out additionally. A special video extensometer (VE) was used to obtain the true stress strain curve. The VE is able to measure the strain in both length and

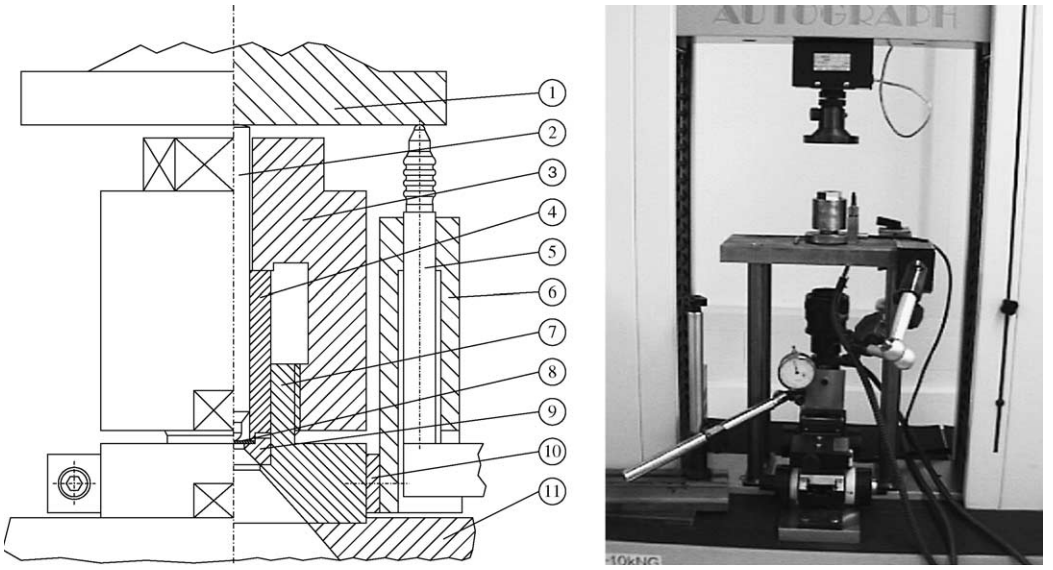

Fig. 1. Cross-section of the loading device and experimental setup of the SPT: (1) cross-head punch of testing machine, (2) punch, (3) housing (upper part), (4) down-holder, (5) position encoder, (6) holder, (7) housing (bottom part), (8) specimen, (9) die, (10) clamp, (11) ground plate.

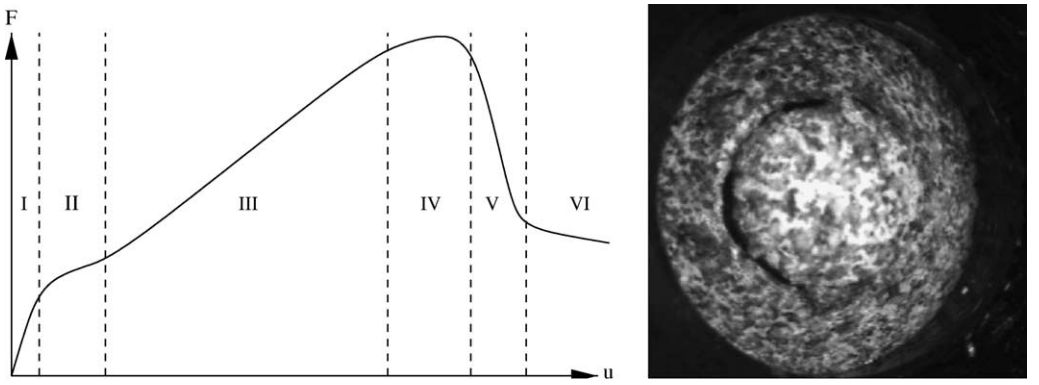

Fig. 2. Load displacement curve and deformed specimen after failure (seen with one of the CCD-cameras).

cross-direction. Furthermore, the radius of curvature on the necking notch ground can be measured and the influence of triaxiality using the Bridgman [23] formula

$$\sigma_{w_{\text{Bridgman}}} = \frac{4F}{\pi d^2}\left[1+\frac{4r}{d}\right]\ln\left[1+\frac{d}{4r}\right] \quad (1)$$

can be taken into account. Here F denotes the tensile force, d the lowest actual diameter and r the radius of curvature on the notch ground. The tensile tests were performed only with specimens of the materials 18Ch2MFA and StE-690.

3. Numerical simulations

After extensive preliminary investigations, the finite element model shown in Fig. 4 was selected,

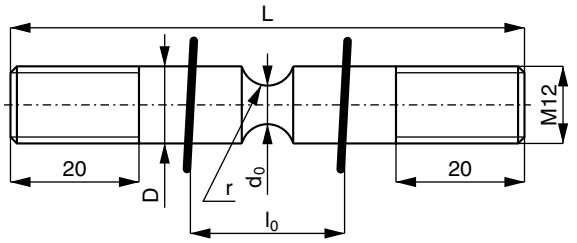

Fig. 3. Notched tensile specimen with marks for strain measure.

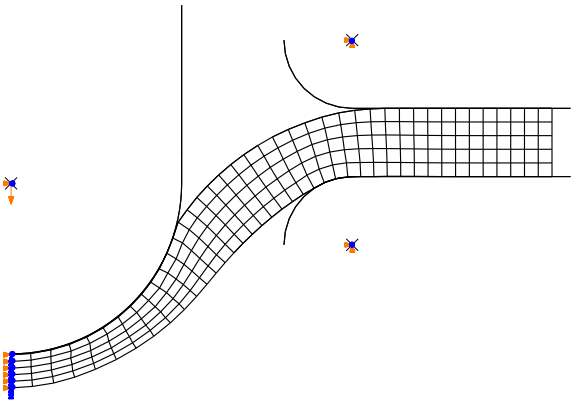

Fig. 4. Finite element model of the SPT.

which delivers the necessary accuracy by reasonable calculation costs. Since the geometries and the load of the SPT are axisymmetric, a two dimensional finite element model is sufficient. The mesh contains 40×5 axisymmetric reduced integration elements, whereby all elements have a size of 0.1×0.1 mm. The die, down-holder and punch are modeled as rigid bodies each one constrained on a master node. Die and down-holder are fixed in all degrees of freedom, whereas the punch can be moved vertically by a displacement boundary condition. The contact between specimen and punch, die and down-holder is modelled including friction whereas the friction coefficient μ can be varied. It should be pointed out that the simulations where performed using the FE-code ABAQUS/Explicit [24] which works with finite deformations in the current configuration, relating the corotational Green–Naghdi stress rate with the rate of deformation according to the GTN constitutive law by a hypoelastic approach, which is already implemented into ABAQUS/Explicit. Since the experimental test lasts approximately two minutes and according to the very small time increments that have to be used with an explicit code, one gets a large computational burden. There are two ways to reduce this computational costs, time scaling or mass scaling. Here, mass scaling was used carefully to keep the influence of dynamic effects as low as necessary.

3.1. Material model

The material model is based on the constitutive damage law developed by Gurson, Tveergard and Needleman (GTN) [19–21,25]. This model assumes spherical voids in an elastic plastic continuum where the voids can grow and nucleate. The void volume fraction f is used as a measure of damage. The central part of the model is the yield function

$$\Phi = \left[\frac{\Sigma_{\mathrm{V}}}{\sigma_{\mathrm{F}}(\varepsilon_{\mathrm{pl}})}\right]^2 + 2q_1 f^* \cosh\left[\frac{3}{2}q_2\frac{\Sigma_{\mathrm{H}}}{\sigma_{\mathrm{F}}(\varepsilon_{\mathrm{pl}})}\right] - (1+q_3 f^{*2}) = 0 \tag{2}$$

where $\Sigma_{\mathrm{V}} = \sqrt{\frac{3}{2}\Sigma'_{ij}\Sigma'_{ij}}$ denotes the v. Mises stress and $\Sigma_{\mathrm{H}} = \frac{1}{3}\Sigma_{kk}$ the hydrostatic stress, expressed by the macroscopic (deviatoric) Cauchy stresses $\Sigma_{ij}(\Sigma'_{ij})$. The damage variable is denoted with f^* and q_1, q_2, q_3 are parameters to weight the different terms of the yield function. The isotropic hardening behavior of the matrix material is denoted with $\sigma_{\mathrm{F}}(\varepsilon_{\mathrm{pl}})$. Up to the initial yield stress R_{e} the material remains purely elastic. Above R_{e} the yield stress σ_{F} is a function of the plastic strain $\varepsilon_{\mathrm{pl}}$ with the parameters R_{e}, ε^* and n.

$$\sigma_{\mathrm{F}}(\varepsilon_{\mathrm{pl}}) = R_{\mathrm{e}}\left[\frac{\varepsilon_{\mathrm{pl}}}{\varepsilon^*}+1\right]^{1/n} \tag{3}$$

ε^* can be expressed as

$$\varepsilon^* = \frac{\varepsilon^*_{\mathrm{pl}}}{\left[\frac{\sigma^*}{R_{\mathrm{e}}}\right]^n - 1} \tag{4}$$

where $\varepsilon^*_{\mathrm{pl}} = 1$ and $\sigma^* = \sigma_{\mathrm{F}}(\varepsilon^*_{\mathrm{pl}})$. In Eq. (2) the damage parameter f^* depends on the void volume fraction f

$$f^* = \begin{cases} f & \text{if } f \leqslant f_c \\ f_c + \frac{f_f^* - f_c}{f_f - f_c}(f - f_c) & \text{if } f_c < f < f_f \\ f_f^* & \text{if } f \geqslant f_f \end{cases} \tag{5}$$

with

$$f_f^* = \frac{q_1 + \sqrt{q_1^2 - q_3}}{q_3} \tag{6}$$

In the above relationship, f_c is a critical value of the void volume fraction, and f_f is the ultimate value of void volume fraction where the material completely fails. The macroscopic plastic Euler–Almansi strain rate $\dot{E}_{ij}^{pl}$ is assumed to be normal to the yield surface

$$\dot{E}_{ij}^{pl} = \dot{\lambda}\frac{\partial \Phi}{\partial \Sigma_{ij}} \tag{7}$$

where $\dot{\lambda}$ denotes the plastic multiplier. The evolution of the equivalent plastic strain in the matrix material is obtained from the equivalent plastic macroscopic work expression

$$(1-f)\sigma_F \dot{\bar{\varepsilon}}_m^{pl} = \Sigma_{ij}\dot{E}_{ij}^{pl} \tag{8}$$

with the equivalent plastic strain

$$\bar{\varepsilon}^{pl} = \bar{\varepsilon}^{pl}\Big|_0 + \int \frac{\Sigma_{ij}\dot{E}_{ij}^{pl}}{(1-f)\sigma_F} \tag{9}$$

The change in void volume fraction is

$$\dot{f} = \dot{f}_{gr} + \dot{f}_{nucl} \tag{10}$$

where $\dot{f}_{gr}$ is the change due to void growth and $\dot{f}_{nucl}$ due to nucleation of new voids. The void growth is based on the law of conservation of mass

$$\dot{f}_{gr} = (1-f)\dot{E}_{kk}^{pl} \tag{11}$$

and the nucleation of voids follows the strain controlled relationship

$$\dot{f}_{nucl} = A\dot{\bar{\varepsilon}}^{pl} \tag{12}$$

with

$$A = \frac{f_N}{s_N\sqrt{2\pi}} \exp\left[-\frac{1}{2}\left(\frac{\bar{\varepsilon}^{pl} - \varepsilon_N}{s_N}\right)^2\right] \tag{13}$$

The normal distribution of the nucleation strain has a mean value ε_N and a standard deviation s_N. f_N denotes the volume fraction of void seeds.

4. Parameter identification

First of all an overview is given about all the different geometric and material parameters that are involved in the finite element model of the SPT. During preliminary investigations concerning the geometry of the specimen and the loading device the values as listed in Table 1 were found to be suitable for the needs of a material parameter identification. Thus we can assume this geometric parameters as fixed. Furthermore, we concentrate on ductile materials with a hardening behavior that follows Eq. (3). The elastic properties and friction coefficients are known for the materials used here, thus have not to be determined, too. The initial void volume fraction f_0 can be determined in many cases by the chemical composition of the material. The percentage of carbon in GGG-40 is manifested as small spherical inclusions which can be treated as voids. Following a suggestion by Franklin [26], f_0 can be estimated for steels by the amount of sulfur and manganese that induce non-metallic inclusions. The void volume fraction at final failure f_f is material dependent and can be measured by microscopic investigations of the crack surfaces. The parameters q_1, q_2 and q_3 are fixed to the values given in Table 1 according to a suggestion given in [27]. The load displacement curve is very insensitive to the parameters ε_N and s_N, why they are fixed to 0.3 and 0.1. Under these assumptions there remain three parameters for the hardening behavior (R_e, σ^*, n) and two (f_c, f_N) for the damage model to be identified by the neural network.

4.1. The identification procedure

The scheme of the identification procedure can be seen in Fig. 5. We start with finite element simulations (lower left) of the SPT using systematically varied sets of material parameters. Each simulation calculates the global load displacement curve $f(u)$ of the punch. This function is stored tabular as a discrete number of n pairs (f_i, u_i), where $f_1 = f(u = 0\text{ mm})$ and $f_n = f(u^{max} = 2\text{ mm})$. This given tabular function is converted into a force vector

Table 1
Parameters of the finite element model of the SPT

Parameter	Id	Description	Value
Geometric			
Specimen	D	Diameter	8.00 mm
	h	Thickness	0.50 mm
Device	d	Die diameter	4.00 mm
	r	Die edge radius	0.50 mm
	R	Punch radius	1.25 mm
Material			
Elastic	E	Young's modulus	≈200 GPa
	h	Poisson's Ratio	0.30
Plastic	R_e	Yield stress at $\varepsilon_{pl} = 0$	50–1000 MPa
	σ^*	Yield stress at $\varepsilon_{pl} = 1$	300–2000 MPa
	n	Hardening coefficient	3–20
Friction	μ	Friction coefficient	0.15
Damage	f_0	Initial vvf	0–15%
	f_c	Critical vvf	0–f_f
	f_N	vvf due to nucleation	0–f_f
	f_f	vvf at final failure	1–100%
	q_1	Parameter of the yield function	1.5
	q_2	Parameter of the yield function	1.0
	q_3	Parameter of the yield function	2.25
	ε_N	Mean nucleation stress	0.3
	s_N	Standard dev. for nucleation	0.1

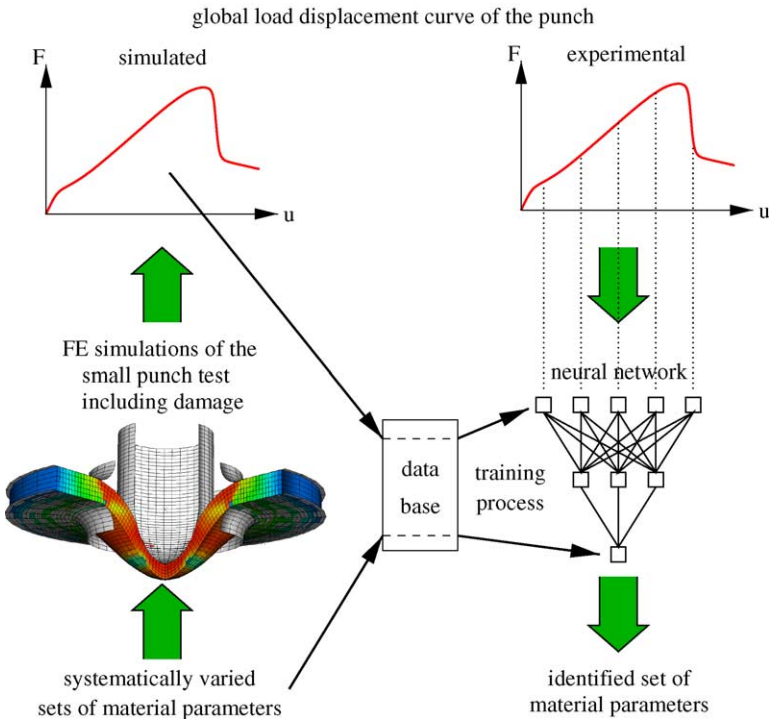

Fig. 5. Scheme of the identification procedure.

$$F_j = f_i + \frac{f_{i+1} - f_i}{u_{i+1} - u_i}(u_j - u_i) \tag{14}$$

with

$$u_j = \frac{j-1}{m} u^{\max} \quad \text{and} \quad u_i \leqslant u_j < u_{i+1} \tag{15}$$

where m denotes the integer number of elements of F. The corresponding parameters par_k and the force vector F_j are normalized using

$$\mathrm{out}_k = \frac{\mathrm{par}_k}{\mathrm{par}_k^{\mathrm{norm}}}, \quad \mathrm{ex}_i = \frac{F_i}{F^{\mathrm{norm}}} \tag{16}$$

Both vectors are stored in a data base, which is used to train a neural network. During a training process (see Section 4.2) the neural network generates an approximated function $\mathrm{out}_k = f(\mathrm{ex}_i)$, where out_k represents the normalized material parameters and ex_i the normalized load displacement curve. This function can be used to identify unknown material parameters out of an experimentally ascertained load displacement curve. The following table presents the values for normalizing the in- and output of the neural network.

F^{norm}	$R_{\mathrm{e}}^{\mathrm{norm}}$	$\sigma^{*\mathrm{norm}}$	n^{norm}	$f_{\mathrm{c}}^{\mathrm{norm}}$	$f_{\mathrm{N}}^{\mathrm{norm}}$
2500 N	800 MPa	1200 MPa	20	0.5	0.1

4.2. The neural network

The neural network that is used here belongs to the class of multi-layer perceptrons or feed forward neural networks [17,18]. It contains three layers of neurons (or units) each having an activation function (see Fig. 6)

$$a_i = \frac{1}{1 + \mathrm{e}^{-\mathrm{net}_i}} \tag{17}$$

where net_i denotes the input for unit i. All units of the input layer get an external input ex_i, which represents in our case the discretisized load displacement curve. In other words, each input ex_i represents the punch force value for a certain load step. The accumulated and with ω_{ij} weighted activations a_i serve as input for the second (hidden) layer.

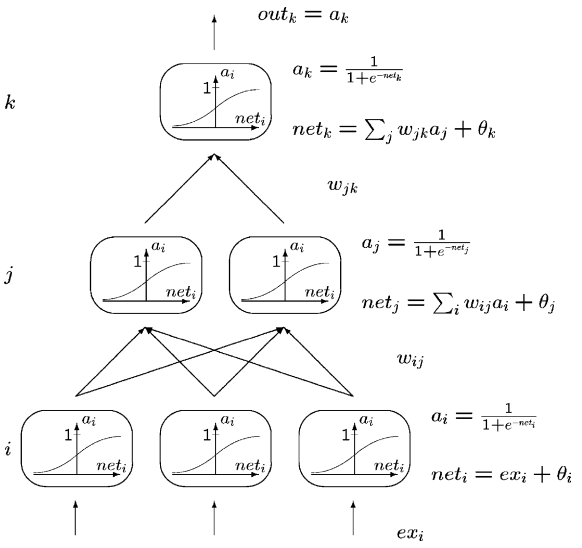

Fig. 6. Scheme of a multi-layer perceptron (feed forward neural network).

$$\mathrm{net}_j = \sum_i \omega_{ij} a_i + \theta_j \tag{18}$$

The input for the third (output) layer comes via the weights ω_{jk} from the hidden layer. The output out_k finally represents the normalized values of the material parameters par_k.

The training procedure is done by changing the weights between the layers with an appropriate learning function. Different training algorithms are known [28] and have been tested (see Fig. 7). The lowest mean square error (MSE) after 1000 training cycles was reached with the scaled conjugate algorithm (SCG). The backpropagation algorithm reached nearly the same accuracy but runs faster then the SCG. Finally the resilent propagation (RPROP) algorithm has been tested, which delivers the poorest accuracy. To check the accuracy of the network for unknown data a validation data set is used. This data set contains an arbitrarily chosen subset of the simulated data which was not part of the training pattern.

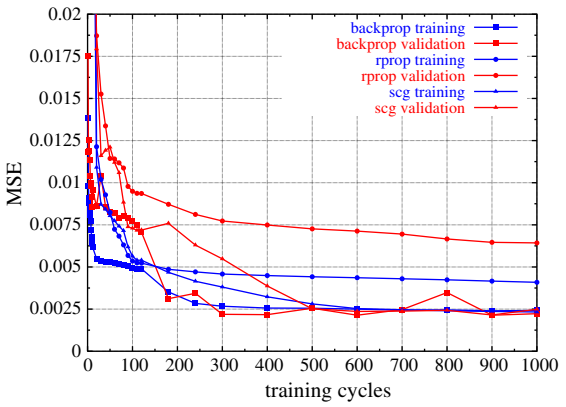

Fig. 7. Mean square error (MSE) for different training procedures. (For this figure and all subsequent figures in colour the reader is referred to the Web version of this article.)

Therefore, we favoured the back propagation algorithm [28], which works as follows: Initially, all weights get a random value in the range [−0.1, 0.1]. An input pattern (discretisized load displacement curve) is feed into the network and propagated forward until it reaches the output layer. The difference or error δ_k between the output a_k and the target output out_k (normalized material parameter used for the simulation) of the training pattern for the output unit k is used together with the activation of the source unit a_j to compute the necessary change of the weight ω_{jk}. To compute the errors for the hidden and input layers, for which no teaching value is available, the δ_k of the following layers which are already computed are used. The second term in Eq. (19) called the momentum term considers the change of weights from the previous training step.

$$\Delta\omega_{ij} = \eta\delta_j a_i + \mu\Delta_{(t-1)}w_{ij} \tag{19}$$

$$\delta_j = \begin{cases} f_j'(\mathrm{net}_j)(\mathrm{out}_k - a_k) & \text{if unit } j \text{ is an output unit} \\ f_j'(\mathrm{net}_j)\sum_k \delta_k w_{jk} & \text{if unit } j \text{ is a hidden unit} \end{cases} \tag{20}$$

$$f_j'(\mathrm{net}_j) = \frac{\partial a_j}{\partial \mathrm{net}_j} \tag{21}$$

5. Results

Fig. 8 shows the computed void volume fraction at different stages of loading. Damage occurs on the bottom side of the specimen about 1 mm out of center of the specimen and grows across the specimen until complete failure. The same position of the ductile crack can be observed at Fig. 2, which shows the bottom face of the specimen seen with one of the CCD-cameras. In the case of tensile specimens (see Fig. 9) damage occurs first in the center of the specimen and grows like a penny shaped crack until the whole cross-section of the specimen has failed.

Fig. 10 shows three different load displacement curves corresponding to three different materials. Here the significant differences in all parts of the load displacement curves become visible.

The result of a first parameter identification for 10MnMoNi55 is shown in Fig. 11. The experimental result is compared with the simulated load displacement curve calculated by using the identified material parameters:

f_c	f_N	R_e	σ^*	n
0.171	0.047	129 MPa	1069 MPa	7.96

These parameters were found using a neural network containing 101 input units, 25 hidden units and 5 output units. This neural network was trained with $5^5 = 3125$ simulated load displacement curves, where

E	f_0	f_f	q_1	q_2	q_3	ε_N	s_N
206.5 GPa	0.002	0.2	1.5	1.0	2.25	0.3	0.1

were hold constant. The curve (data base) in Fig. 11 represents that one of the training curves that fits the experiment best.

Investigations for the material 18Ch2MFA yielded the following parameter set, which fits equally well both the small punch and tensile test results (see Figs. 12 and 13).

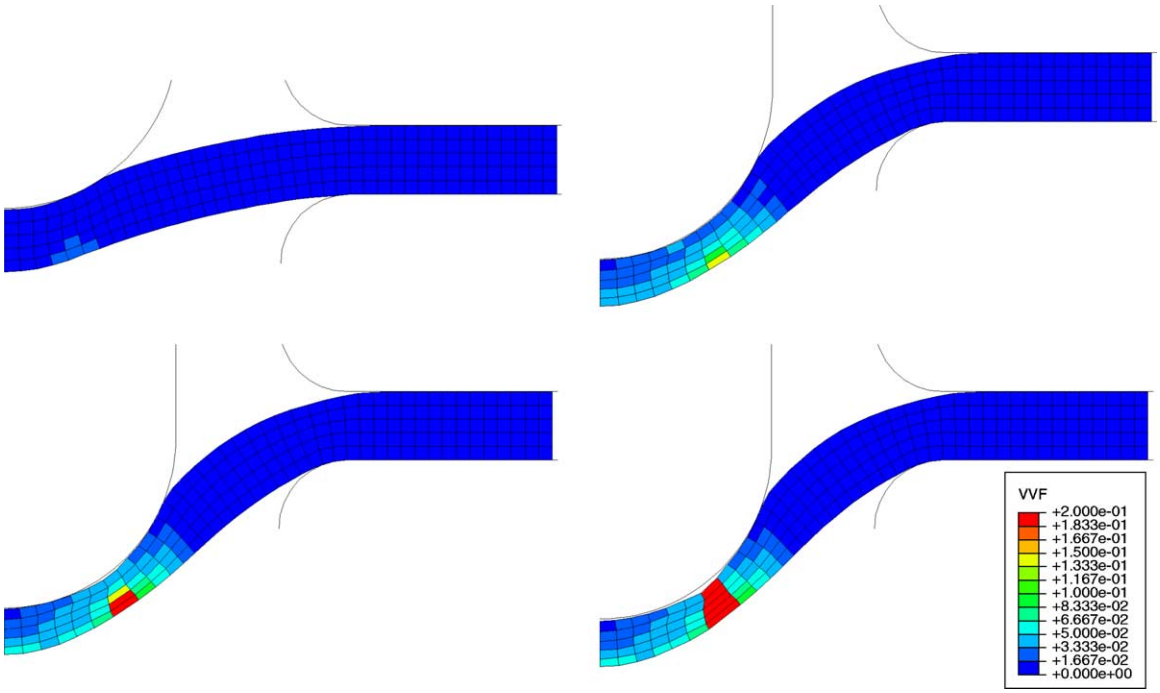

Fig. 8. Evolution of the void volume fraction (damage) in a small punch specimen.

E	R_e	σ^*	n
210 GPa	129 MPa	900 MPa	20

f_0	f_c	f_f	q_1	q_2	q_3	f_N	ε_N	s_N
0.002	0.062	0.2	1.5	1.0	2.25	0.03	0.3	0.1

E	R_e	σ^*	n
210 GPa	150 MPa	1100 MPa	14

f_0	f_c	f_f	q_1	q_2	q_3	f_N	ε_N	s_N
0.002	0.0084	0.012	1.5	1.0	2.25	0.0	0.0	0.0

The maximum load for the small punch test is slightly underestimated, whereas the point of failure is predicted very well. The parameter set given above simulates the tensile specimen with notch radius 4 and 8 mm very well. For the smaller notches the failure point is estimated at higher strains and for the unnotched specimen the simulated failure occurs too early.

For the StE-690 the following parameter set was found to predict the small punch test as well as the tensile tests (see Figs. 14 and 15):

Here, no void nucleation is simulated, therefore the parameters having the index N remain zero. To estimate the point of failure right, the values for f_c and f_f have to be very low, much lower than one would expect from a physical point of view.

6. Conclusions

A new approach is developed to identify deformation and failure properties of ductile materials

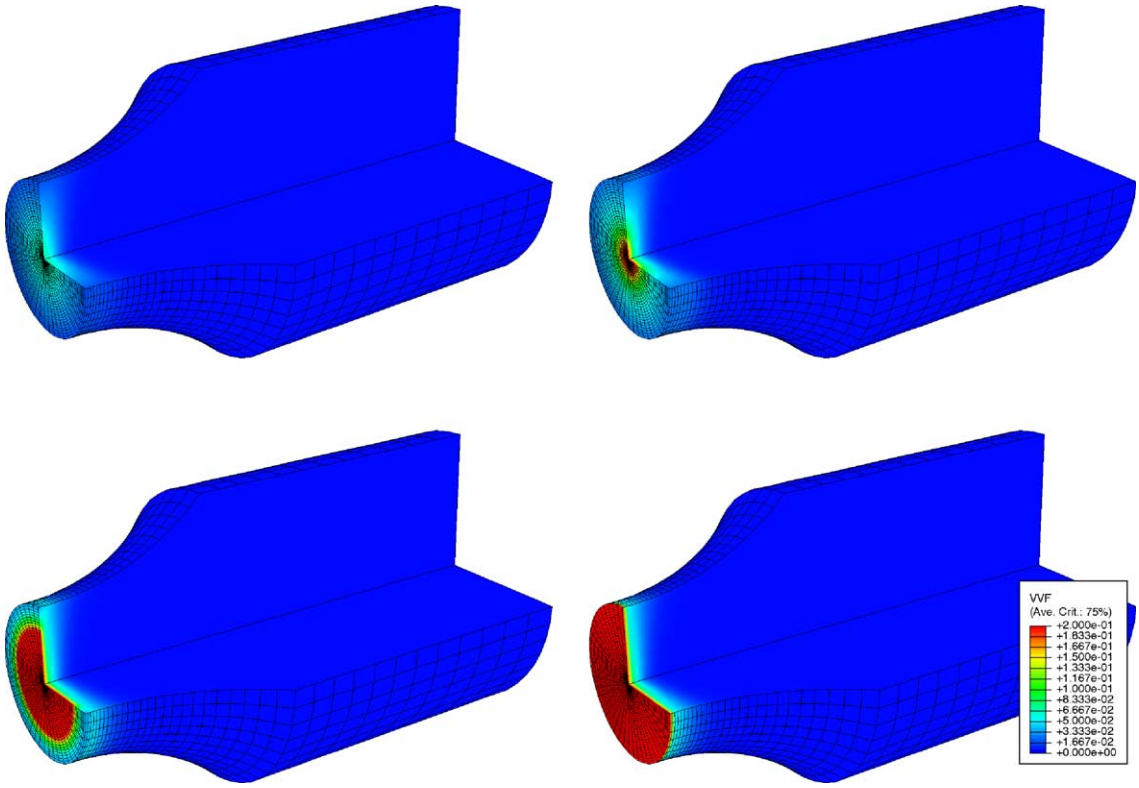

Fig. 9. Evolution of the void volume fraction (damage) in a tensile specimen.

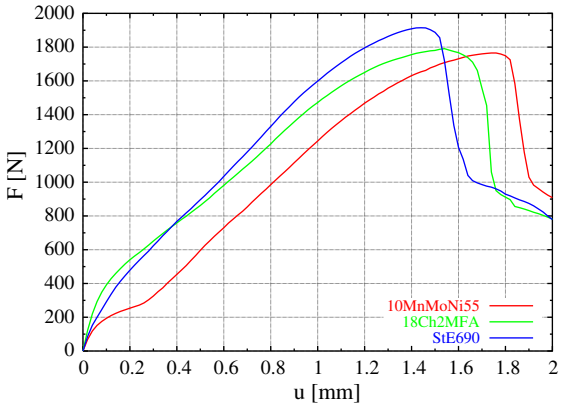

Fig. 10. Experimental small punch load displacement curves of different materials.

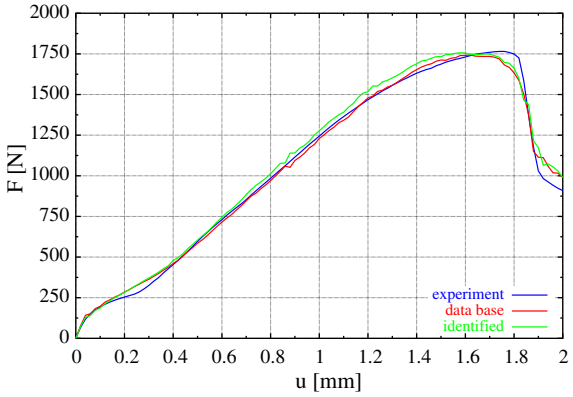

Fig. 11. Simulated load displacement curves of 10MnMoNi55.

by exploiting the experimental results of the small punch test. The set up of the technical device for determining the load displacement curve of the SPT is described in detail.

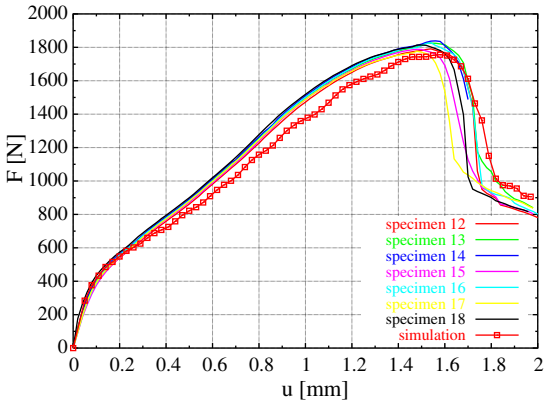

Fig. 12. Small punch test 18Ch2MFA.

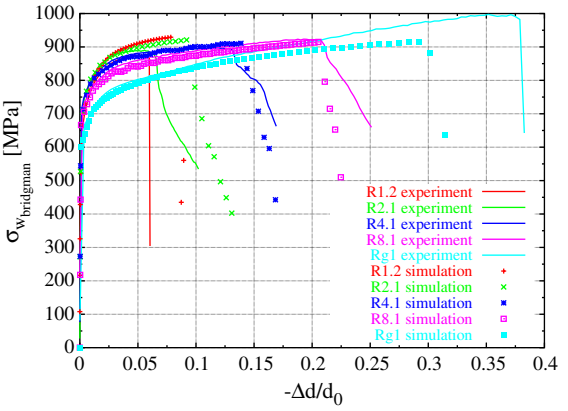

Fig. 13. Tensile test 18Ch2MFA.

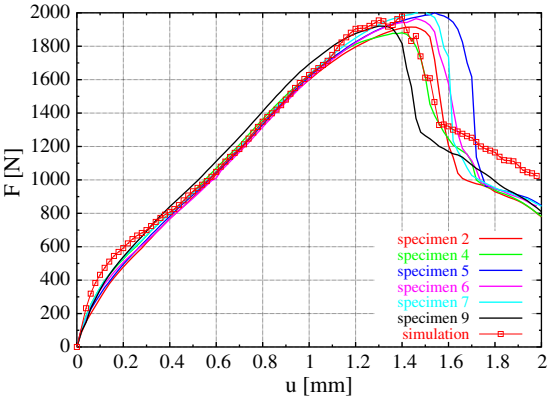

Fig. 14. Small punch test StE-690.

As has been shown, neural networks are able to generate an approximated function for the material parameters depending on the shape of the load displacement curve of the punch. This function is obtained during a training process with results from numerical simulations using the GTN-material model. It is necessary to make pre-selection of the parameters, which have to be identified because an identification of all 12 GTN-Parameters is too complex. This pre-selection is depending on the type of material.

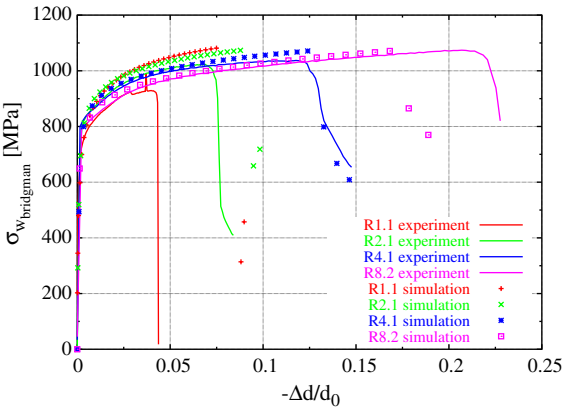

Fig. 15. Tensile test StE-690.

For the three different steels 10MnMoNi55, 18Ch2MFA and StE690, sets of material parameters have been found that determine the material behavior reasonably well. For the 18Ch2MFA and StE690 material this parameters could be verified by experiments and simulations of notched tensile specimens using the same parameters. In exceptional cases the values for the critical and ultimate void volume fraction do not agree with values one would expect from a physical point of view. Since the GTN-model assumes that only spherical void growth and nucleation cause damage and neglects all other influences, the void volume fraction should be understood as a phenomenological damage variable. Anyway, it has be demonstrated that this damage model can predict the ductile deformation and failure of metals very well for quite different stress states.

Acknowledgements

This work is gratefully funded by the German Research Foundation (DFG) under contract Ku

929/5. The useful comments of the unknown reviewer are acknowledged by the authors.

References

[1] M. Manahan, A. Argon, O. Harling, The development of a miniaturized disc bend test for the determination od postirradiation mechanical properties, Journal of Nuclear Materials 103–104 (ggf. Teil B) (1981) 1545–1550.

[2] J. Foulds, C. Jewett, L. Bisbee, T. Gabel, R. Viswanathan, In-service steam turbine rotor material evaluation by small punch testing, in: Steam Turbine-Generator Developments for the Power Generation Industry, vol. 18, American Society of Mechanical Engineers, Power Division (Publication) PWR, 1992, pp. 151–157.

[3] S. Jitsukawa, M. Kizaki, A. Umino, K. Shiba, A. Hishinuma, Methods and devices for small specimen testing at the Japan Atomic Energy Research Institute, in: ASTM Special Technical Publication, 1204, ASTM, 1993, pp. 289–307.

[4] J.-M. Baik, J. Kameda, O. Buck, Small punch test evaluation of intergranular embrittlement of an alloy steel, Scripta Metallurgica 17 (1983) 1443–1447.

[5] J.-M. Baik, J. Kameda, O. Buck, Development of small punch tests for ductile–brittle transition temperature measurement of temper embrittled Ni–Cr steels, in: The Use of Small Specimens for Testing Irradiated Materials, Philadelphia, PA, USA, 1986, pp. 92–111.

[6] S.-H. Chi, J.-H. Hong, I.-S. Kim, Evaluation of irradiation effects of 16 MeV proton-irradiated 12Cr–1MoV steel by small punch (SP) tests, Scripta Metallurgica et Materialia 30 (12) (2000) 1521–1525.

[7] M. Eto, H. Takahashi, T. Misawa, M. Suzuki, Y. Nishiyama, K. Fukaya, S. Jitsukawa, Development of a miniaturized bulge test (small punch test) for post-irradiation mechanical property evaluation, in: ASTM Special Technical Publication, 1204, ASTM, 1993, pp. 241–255.

[8] X. Mao, J. Kameda, Small-punch technique for measurement of material degradation of irradiated ferritic alloys, Journal of Materials Science 26 (1991) 2436–2440.

[9] E. Fleury, J. Ha, Small punch tests to estimate the mechanical properties of steels for steam power plant: I. Mechanical strength, International Journal of Pressure Vessels and Piping 75 (9) (1998) 699–706.

[10] J. Bulloch, Toughness losses in low alloy steels at high temperatures: an appraisal of certain factors concerning the small punch test, International Journal of Pressure Vessels and Piping 75 (11) (1998) 791–804.

[11] X. Mao, H. Takahashi, T. Kodaira, Estimation of mechanical properties of irradiated nuclear pressure vessel steel by use of subsized ct specimen and small punch specimen, Scripta Metallurgica et Materialia 25 (11) (1991) 2487–2490.

[12] A.N. Sinclair, O. Lepik, M. Gabbani, B. Mukherjee, E. Albertini, Assessment of fracture toughness by a punch test with miniature specimens, in: Small Specimen Test Techniques Applied to Nuclear Reactor Vessel Thermal Annealing and Plant Life Extension, STP 1204, New Orleans, Luisiana, USA, 1993, pp. 162–181.

[13] Y. Xu, Z. Zhao, A modified miniature disk test for determining material mechanical properties, Journal of Testing and Evaluation 23 (4) (1995) 300–306.

[14] X. Mao, M. Saito, H. Takahashi, Small punch test to predict ductile fracture toughness J_{Ic} and brittle fracture toughness K_{Ic}, Scripta Metallurgica et Materialia 25 (11) (2000) 2481–2485.

[15] C. Sainte Catherine, J. Messier, P. Christophe, S. Rosinski, J. Foulds, EPRI-CEA finite element simulation benchmark and inverse method for the estimation of elastic plastic behavior, in: Small Specimen Test Techniques, ASTM STP 1418, vol. 4, ASTM International, 2002, pp. 350–370.

[16] N. Huber, C. Tsakmakis, Determination of constitutive properties of thin metallic films on substrates by spherical indentation using neural networks, International Journal of Solids and Structures 37 (2000) 6499–6516.

[17] H.B. Keller, Maschinelle Intelligenz, Verlag Vieweg, 2000.

[18] D. Nauck, F. Klawonn, R. Kruse, Neuronale Netze und Fussy-Systeme, Verlag Vieweg, 1994.

[19] A.L. Gurson, Continuum theory of ductile rupture by void nucleation and growth: Part I—Yield criteria and flow rules for porous ductile materials, Journal of Engineering Materials and Technology 99 (1977) 2–15.

[20] A.L. Gurson, Porous rigid-plastic materials containing rigid inclusions-yield function, plastic potential and void nucleation, Fracture 2 (1977) 357–364.

[21] V. Tvergaard, Influence of voids on shear band instabilities under plane strain conditions, International Journal of Fracture Mechanics 17 (1981) 389–407.

[22] M. Erbe, K. Galanulis, R. Ritter, E. Steck, Theoretical and experimental investigations of fracture by finite element and grating methods, Engineering Fracture Mechanics 48 (1994) 103–118.

[23] P.W. Bridgman, Studies in Large Plastic Flow and Fracture, McGraw-Hill Book Company Inc., New York, Toronto, London, 1952.

[24] ABAQUS Theory Manual, Hibbitt, Karlsson & Sorensen, Inc. USA, 2001.

[25] ABAQUS/Explicit User's Manual Vol. II Version 6.2, Hibbitt, Karlsson & Sorensen, Inc. USA, 2001.

[26] A. Franklin, Comparison between a quantitative microscope and chemical methods for assessment of non-metallic inclusions, Journal of the Iron and Steel Institute (1969) 181–186.

[27] G. Bernauer, W. Brocks, U. Muehlich, D. Steglich, M. Werwer, Hinweise zur Anwendung des Gurson–Tvergaard–Needleman-Modells, Technical note gkss/wmg/99/10, GKSS-Forschungszentrum Geesthacht (1999).

[28] A. Zell et al., SNNS Stuttgart Neural Network Simulator, User Manual, Version 4.1, 1995.